Nanoscale

Accepted Manuscript

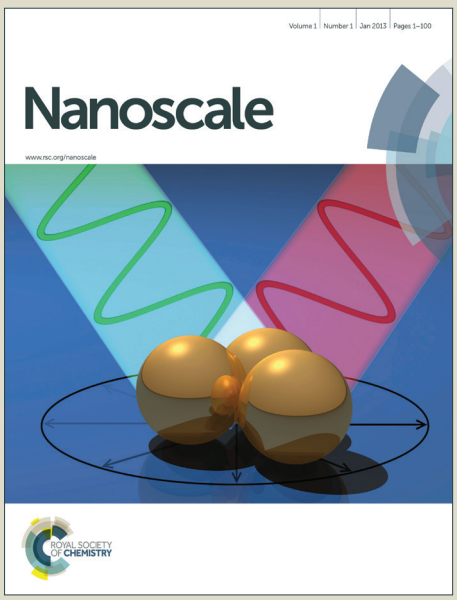

This is an *Accepted Manuscript*, which has been through the Royal Society of Chemistry peer review process and has been accepted for publication.

Accepted Manuscripts are published online shortly after acceptance, before technical editing, formatting and proof reading. Using this free service, authors can make their results available to the community, in citable form, before we publish the edited article. We will replace this *Accepted Manuscript* with the edited and formatted *Advance Article* as soon as it is available.

You can find more information about *Accepted Manuscripts* in the Information for Authors.

Please note that technical editing may introduce minor changes to the text and/or graphics, which may alter content. The journal's standard Terms & Conditions and the Ethical guidelines still apply. In no event shall the Royal Society of Chemistry be held responsible for any errors or omissions in this *Accepted Manuscript* or any consequences arising from the use of any information it contains.

ROYAL SOCIETY OF CHEMISTRY

www.rsc.org/nanoscale

Cite this: DOI: 10.1039/c0xx00000x

www.rsc.org/xxxxxx

ARTICLE TYPE

Correlative electron and X-ray microscopy: Probing chemistry and bonding with high spatial resolution

Angela E. Goode,*[a] Alexandra E. Porter,[a] Mary P. Ryan[a] and David W. McComb*[b]

Received (in XXX, XXX) Xth XXXXXXXXX 20XX, Accepted Xth XXXXXXXXX 20XX

DOI: 10.1039/b000000x

Two powerful and complementary techniques for chemical characterisation of nanoscale systems are electron energy-loss spectroscopy in the scanning transmission electron microscope, and X-ray absorption spectroscopy in the scanning transmission X-ray microscope. A correlative approach to spectro-microscopy may not only bridge the gaps in spatial and spectral resolution which exist between the two instruments, but also offer unique opportunities for nanoscale characterisation. This review will discuss the similarities of the two spectroscopy techniques and the state of the art for each microscope. Case studies have been selected to illustrate the benefits and limitations of correlative electron and X-ray microscopy techniques. *In situ* techniques and radiation damage are also discussed.

Introduction

Growth in the development and applications of nanotechnology brings with it an increasing need for characterisation methods capable of providing both structural and chemical analysis on the nanometre scale. Most laboratory based characterisation techniques such as ultra-violet and infra-red spectroscopies, mass spectrometry and thermogravimetric analysis provide spatially averaged information from comparatively large volumes of sample. While these techniques provide a representative overview of the sample, their averaged signals often probe not only the nanomaterial of interest, but also any support material, debris and impurities in heterogeneous structures. In addition, averaged properties miss statistical outliers, which may be critical for the function of the nanomaterial. For characterisation of interfaces or individual nanostructures, techniques with much higher spatial resolutions are essential.

There are few available techniques capable of providing chemical information on the nanometre scale. This review will discuss two such methods: electron energy-loss spectroscopy in the scanning transmission electron microscope (STEM-EELS) and X-ray absorption spectroscopy in the scanning transmission X-ray microscope (STXM-XAS). These spectroscopies study the primary processes of inelastic electron scattering or X-ray absorption to obtain chemical information, from chemical speciation analysis to local bonding environments and electronic structure. While the secondary process of X-ray emission also provides chemical information in the electron and X-ray microscopes (by energy dispersive X-ray spectroscopy and X-ray probe X-ray micro- and nano-analysis respectively), these techniques, whilst being very sensitive to low concentrations, are limited to *elemental* analysis, and they will not be discussed in this review. Although the probe-specimen interactions of EELS and XAS differ (electron scattering and photon absorption, respectively), they provide remarkably similar chemical information. Due to recent advances in diffractive optics for soft (100 eV to 2 keV[1]) X-rays, as well as monochromators and aberration correctors for electron microscopes, the spatial and spectral resolutions of STXM-XAS and STEM-EELS are converging. However, the fundamental diffraction limit for X-rays means STXM-XAS cannot match the spatial resolution of STEM-EELS, while it is unlikely that the combined high flux and high energy-resolution achievable in synchrotron based X-ray microscopes will ever be matched in the electron microscope. Additionally, differences in primary damage mechanisms and detection efficiencies alter the suitability of each technique for different samples. Thus, a correlative approach that brings together STXM-XAS and STEM-EELS will be very powerful for bridging the gaps in spatial and spectral resolutions between these techniques, allowing new insights to be gained into nanostructured systems.

Core loss energy-loss events studied in a high voltage (60–300 kV) electron microscope typically range from about 50 eV to 2000 eV, which corresponds well with the energy of soft X-rays (100-2000 eV), and covers edge onsets for many of the elements in the periodic table.[2] Below this energy range, between ~1 and 50 eV, spectral features arise from excitations of valence electrons. Such transitions are often studied by low-loss (or valence-loss) (V)EELS, however the photon spectroscopy equivalent lies in the IR-visible-UV range, where diffraction-limited spatial resolutions are at least an order or magnitude poorer than soft X-rays and do not constitute nanoscale spectroscopy. Conversely, energy-loss events above 2000 eV become increasingly difficult to detect by EELS due to small scattering cross-sections and large backgrounds.[2] These transitions are more easily studied by hard X-ray spectroscopy, which provides access to the inner shell ionisation events in heavy elements. This review will concentrate on spectroscopy

Nanoscale Accepted Manuscript

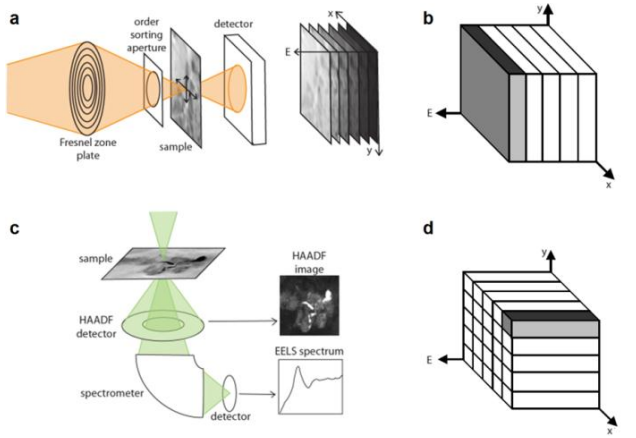

Fig. 1 Schematic of (a) STXM-XAS and (c) STEM-EELS with corresponding diagrams showing the order of data acquisition in (b) a STXM "stack", in which images at different photon energies are acquired sequentially, and (d) an EELS "spectrum image" in which a whole EEL spectrum is acquired at a given position before the probe is moved, and the spectrum acquisition repeated.

between 100 and 2000 eV, corresponding to core-loss EELS and soft X-ray XAS, as this is where the techniques are most comparable. However, there is much to gain from extending the correlative approach beyond this energy range, and we will attempt to highlight areas where incorporating VEELS or hard X-ray spectroscopy may be most beneficial.

In this review we will explain the similarities between XAS and EELS, briefly introduce the two microscopes, and present case studies in which electrons and/or X-rays have been employed to gain understanding of a range of nanostructured systems. The examples discussed have been chosen to illustrate the potential benefits and limitations of a correlative approach, and include a discussion on radiation damage in organic systems. For more comprehensive reviews of the *individual* techniques, readers are referred elsewhere.[3-7]

XA and EEL spectra

In the case of core loss EELS, the incident primary electron interacts with an atomic electron in the specimen, loses some energy (E) and promotes the atomic electron from its initial state into an unoccupied final state. When discussing the probability of this transition, the double-differential cross-section is used. This represents the fraction of electrons that are scattered into a solid angle dΩ with an energy between E and E + dE. The double-differential cross-section can be derived quantum mechanically using Fermi's Golden Rule. Under the one-electron approximation, in which other atomic electrons do not contribute to the excitation process, and the dipole approximation, in which the momentum transferred is small (so that $e^{i\underline{q}.\underline{r}}$ tends to 1 + $\underline{q}.\underline{r}$) the double-differential cross-section takes the form:

$$\frac{d^2\sigma}{dEd\Omega} \propto \frac{4\gamma^2}{a_0{}^2q^4}\left|\left\langle\psi_f\left|\underline{q}\cdot\underline{r}\right|\psi_i\right\rangle\right|^2\rho(E) \qquad (1)$$

Where a_0 is the Bohr radius, γ is the relativistic correction factor, $\underline{q}$ is the scattering vector, $\underline{r}$ is the position of the atomic electron, $|\psi_i\rangle$ and $|\psi_f\rangle$ are the initial and final states and $\rho(E)$ is the density of states.

A photon which is incident on a sample has some probability of being absorbed, causing an inner shell electron to be excited into a higher final state. This probability of absorption is described by the X-ray absorption coefficient μ, whose form may also be derived from Fermi's Golden Rule. For soft X-rays, where the X-ray wavelength is much greater than the extent of the initial state, the probability has the form:

$$\mu \propto \sum_f\left|\left\langle\psi_f\left|\underline{\varepsilon}\cdot\underline{r}\right|\psi_i\right\rangle\right|^2\delta(\hbar\omega - E_f + E_i) \qquad (2)$$

Where $\underline{\varepsilon}$ is the polarization vector of the light, $\underline{r}$ is again the position of the atomic electron and $\delta(\hbar\omega - E_f + E_i)$ is the density of states.

Equations 1 and 2 are similar in that both the electron-electron interaction operator $\underline{q}\cdot\underline{r}$, and the photon-electron operator $\underline{\varepsilon}\cdot\underline{r}$ have a dipole form (within the dipole limit in the case of EELS). Therefore, the selection rules that determine allowed final states are the same *i.e.* the change in angular momentum $\Delta l = \pm 1$. Accordingly, we expect the shape of EEL and XA spectra to be equivalent.

Scanning transmission X-ray and electron microscopes

X-ray microscopes make use of Fresnel zone plates as focusing elements.[8] These diffractive optics consist of concentric alternating transmitting and absorbing rings, and are able to focus X-ray beams to spots of ~ 20 nm in diameter.[8] The STXM was developed in 1985 by Kirz and Rarback,[8] and is shown in figure 1. Monochromated X-rays are focused by the zone plate on to a thin sample which is scanned across the X-ray probe while the transmitted X-ray intensity is detected (figure 1a). An alternative microscope setup involves a full-field configuration in which the entire field of view is illuminated, and transmitted X-rays are imaged using a zone plate and recorded on a position-sensitive detector. Full-field imaging is fast, facilitating both tomography[9] and kinetic studies.[10] However the location of the zone plate after the sample is problematic. These optics have transmission efficiencies of only 10-15%, meaning that much more flux must be incident at the sample compared to that collected at the detector, increasing the dose at the sample. To date, many of the soft X-ray micro-spectroscopy studies have been performed using scanning transmission X-ray microscopes.

In the STXM, an absorption image is usually collected at a single photon energy by recording the transmitted flux while the sample is raster-scanned across the stationary X-ray probe. The photon energy is then changed, another absorption image is recorded, and the process is repeated to build up a three-dimensional data cube or 'stack' (with two spatial dimensions and one energy dimension). The sequence of data acquisition in the STXM is similar to that of energy filtered (EF-) TEM spectrum imaging which may be familiar to the electron microscopist. X-ray absorption is a resonant process and X-rays are either absorbed or not, *i.e.*, the probability of absorption corresponds to the energy differential cross section at a particular energy. This is in contrast to inelastic electron scattering in the TEM, where incident electrons can lose energy in many different ways, corresponding to all the values of the energy-differential cross section across the entire range of energy losses. Therefore the *serial* acquisition of a spectrum is much more efficient for X-rays than for electrons. The EFTEM mode of spectrum imaging is relatively inefficient, as all possible energy-loss events occur

Nanoscale Accepted Manuscript

This journal is © The Royal Society of Chemistry [year]

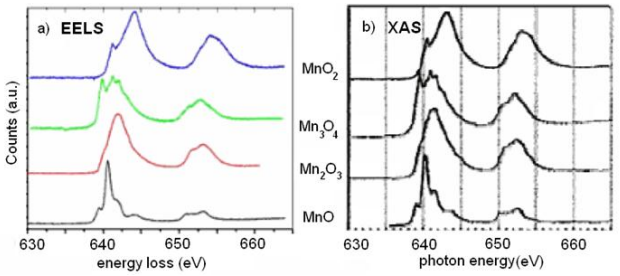

Fig. 2 Fine structure at the Mn $L_{2,3}$ edges of Mn oxides show excellent agreement. ELNES at 0.2 eV resolution (a) compared to XANES with 0.1 eV resolution (b). Reprinted from Walther *et al*., [13] with kind permission from Springer Science and Business Media.

simultaneously and contribute to sample damage, while only a subset contribute to the EFTEM image.

Although the transmitted X-ray intensity is the most direct measure of X-ray absorption, other signals such as total electron yield (TEY) can also be used as an equivalent measure of the absorption signal, especially in samples too thick for X-ray transmission. TEY is a measure of the total current associated with non-radiative decay of core holes and has the advantage of being surface sensitive, however it relies on the assumption that the number of electrons created is proportional to the number of photons absorbed.[11] Some care needs to be taken when comparing EEL and XA spectra acquired using different detection modes, as these can influence the measured spectral shape. For example, when performing TEY measurements on insulating systems, McComb *et al.*[12] found that the charging of insulating ZrO_2 grains during spectrum acquisition modified the relative intensities of the peaks in the X-ray data compared to their ELNES measurements.

In STEM 'spectrum imaging' the electron beam is also focussed to a probe which is scanned over the sample (figure 1c). The transmitted electrons are dispersed according to their energy-loss using a spectrometer, which is commonly a magnetic prism. EEL spectra are acquired in parallel, where the whole spectrum is detected at once on a position sensitive detector. At each probe position a complete EEL spectrum is acquired. By scanning the electron probe across the sample and recording an EEL spectrum at each point, an analogous 3D dataset is acquired, but in a different order to the X-ray dataset (figure1 b,d).

Spectral resolution

The grating monochromators used in soft X-ray beamlines are well-developed.[14] A typical spectral resolving power or monochromaticity (defined as $E/\Delta E$) is ~5000, which corresponds to an energy resolution of 60 meV at the carbon K edge for example, or 140 meV at the iron $L_{2,3}$ edge.[15-17] These values are below the natural widths of core loss spectra,[18] enabling detailed fine structure in the near edge region to be adequately resolved. In this situation, the principle reason to pay attention to energy resolution in the STXM is to enable meaningful comparisons between spectra measured at different facilities.[19] It is worth bearing in mind that using beams of higher than necessary monochromaticity is detrimental since the photon flux will be lowered. In addition, sampling a spectrum at smaller than necessary energy steps will increase the X-ray dose, as X-ray spectra are acquired sequentially. It is common practice in STXM spectroscopy to vary the spectral sampling steps across an edge,

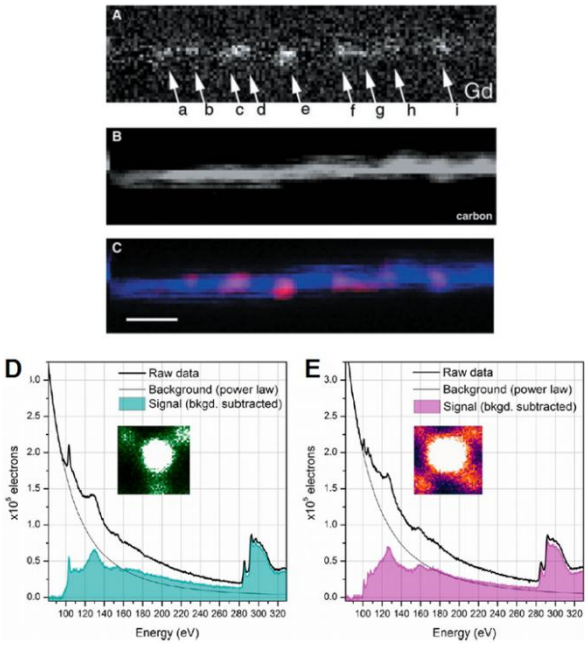

Fig. 3 Examples of single-atom EELS. (a-c) Chemical maps of gadolinium (red) and carbon (blue) calculated from EELS data of Gd-metallofullerene molecules confined in a SWNT. From Suenaga *et al.*[22] Reprinted with permission from AAAS. Points a, b and i indicate single Gd atoms. Scale bar 3 nm. (d-e) EEL spectra of single Si dopant atoms in 3- and 4-fold coordinations in a graphene lattice. Reprinted with permission from Ramasse *et al*.[23] Copyright 2013 American Chemical Society.

with the smallest steps in the near edge region, in order to minimise the dose while resolving near-edge features.

In the TEM, many factors deteriorate the energy resolution of EEL spectra. Energy broadening from electron interactions in the illumination system, the design of the spectrometer, and the stability of power supplies all contribute, but the main limiting factor is the energy spread of the electron source.[20] Thermionic, Schottky-emission and cold field-emission guns have typical energy spreads of 2 eV, 0.7 eV and 0.3 eV, respectively.[2, 21] These energy spreads are greater than many natural line widths, with the result that fine structure is not fully resolved in such EEL spectra, and information about the chemical environments is reduced.

This situation was greatly improved with the introduction of electron monochromators in the 1990s.[24] Monochromators consist of either an omega or a Wein filter, effectively a spectrometer within the illumination system. Monochromators disperse beam electrons and then select a narrow energy range using a slit,[25] improving spectral resolution at the expense of probe current. Typical monochromated instruments allow energy resolutions of ~ 100 meV to be reached, and their introduction has led to huge advances in the detection of EELS fine structure. For example, EEL spectra of single crystal V_2O_5 that were acquired with a monochromated energy resolution of 0.22 eV show additional shoulders in the vanadium $L_{2,3}$ peaks (at ~515 eV) compared with non-monochromated spectra taken with 0.6 eV resolution.[26] XAS measurements of the V_2O_5 crystal were also acquired with a spectral resolution of 0.08 eV. The shoulders observed in the monochromated EEL spectra were clearly resolved as peaks by XAS, but the improved energy resolution

Nanoscale Accepted Manuscript

did not reveal any further structures in the V $L_{2,3}$ edge.

Another study by Walther *et al.*[13] compared monochromated EELS with XA spectra of manganese oxides at the higher energy Mn $L_{2,3}$ edges (~640 eV). In these data, the energy resolutions of the EELS and XAS were 0.2 eV and 0.1 eV, respectively. Both these values are below the ~0.3 eV natural line width of the Mn $L_{2,3}$ edge,[18] explaining the excellent agreement between EELS and XAS at this edge (figure 2). The examples above demonstrate that the spectral performance of monochromated EELS is now competitive with XAS measurements, and that both are capable of resolving the fine structure at core loss edges. Currently a new generation of monochromators are being developed for the TEM, promising huge improvements in energy resolution, down to ~10 meV.[27] While these monochromators will have most impact on the valence-loss region of the EEL spectrum, where vibrational modes may even be resolved,[28] their improved spectral resolution will also benefit lower energy core-loss edges, where the sharpest features are ~100 meV wide and can only just be resolved in current generation monochromated TEMs.[29] Due to the similarities in interaction cross-sections (as long as dipole conditions are met), and comparable spectral resolutions, XAS and EEL spectra should be directly comparable. Any remaining differences between the spectra could be due to differences in spatial resolutions, damage mechanisms or sample environments, which will be discussed in the rest of this article.

Spatial resolution and sensitivity

Another recent advancement in the field of electron microscopy is the development of aberration correctors for electron optics, allowing STEM probes to be focussed to sub-ångström sizes. EEL spectra can be recorded along atomic columns of crystals, showing their elemental compositions,[30, 31] and can even resolve different bonding states, for example at a Si-SiO_2 interface,[32] with atomic-column resolution. In these experiments, the spatial resolution of EELS measurements becomes limited by the delocalisation of inelastic scattering rather than the dimensions of the electron probe.[25, 33] Suenaga *et al.* demonstrated that even single-atom detection is achievable using STEM-EELS (figure 3 a-c). Using a model system of Gd-metallofullerene molecules trapped within a single walled nanotube (SWNT), individual Gd atoms were mapped using the Gd N edge, though counting statistics were understandably low.[22] In a more recent study, Ramasse *et al.*[23] were able to obtain EEL spectra over individual substitutional Si atoms in graphene, and observed changes in fine structure for different defect geometries (figure 3 d,e). Such single-atom EELS studies are often limited by sample instabilities and electron beam damage, even in these relatively ideal systems. In the metallofullerene experiment, Gd atoms were observed to move within their fullerene cages within the short (35 ms) acquisition times,[22] and the silicon dopants in the graphene experiment were occasionally observed to jump to neighbouring sites.[23] As single-atom spectroscopy is limited by these sample instabilities, an increase in probe brightness or acquisition time alone may not be suitable for achieving better signal-to-noise ratios (SNR) or for investigating other elements with lower scattering cross-sections. Instead, improvements in detector sensitivity are required for single-atom measurements to become more routinely achievable in EELS.

While sub-angstrom electron probes are becoming more common in electron microscopy, soft X-ray STXMs are routinely operating at spatial resolutions two orders of magnitude poorer, around 25 nm. Currently the highest reported spatial resolutions in conventional STXMs are 10 nm (with 700 eV X-rays)[34] and 9 nm (with 1200 eV X-rays),[35] and are limited by the ability to fabricate zone plates with narrow outer zone widths of ~10 nm. It is possible to overcome the limitation of X-ray optics using diffraction-based methods such as ptychography, and chemical maps of $LiFePO_4$ have recently been obtained with 5 nm spatial resolution.[36] Concentrations of 0.1-1% are typically detectable by STXM-XAS. Amongst the lowest concentrations to be measured in the STXM is a 2 nm layer of Co within 250 nm of other metals,[37] and a vanadium concentration of 0.23 at% ± 0.05 at% in cometary particles.[38] The limited spatial resolution of STXM means single atom detection is not achievable in the STXM, despite the high chemical sensitivity of this technique. The STXM-XAS detection limit of ~0.1% is expected to improve if one switches from measuring transmission signals, in which the measurement of interest is a small drop in a large number of background counts, to yield techniques such as X-ray fluorescence yield-STXM. X-ray fluorescence yield-STXM is currently being developed, and its increased sensitivity compared to X-ray absorption measurements has already been qualitatively demonstrated in a study of As and Mg in bacterial samples.[41, 42]

Correlative studies

Although STEM-EELS and STXM-XAS are in many ways complementary, and they are frequently used individually to characterise nanoscale systems, there are relatively few examples in the literature in which a single study combines both techniques. More often, (possibly due to the limited availability of STXM beamlines) bulk XAS measurements are combined with TEM analysis which provides the spatially-resolved information of the sample. For example, in a correlative study of vanadium oxide nanotubes, bulk XAS measurements revealed double peaks at 531 and 533 eV in the oxygen K edge, which were used to confirm the chemical speciation of the tubes as V_2O_5.[39] As the EELS measurements were not monochromated and had an energy resolution of 1.1 eV, this fine structure was not resolved, and could only be inferred from the asymmetry in the oxygen edge (figure 4 a,b). EDX and EELS signals were however useful for mapping the distributions of elemental oxygen and vanadium across the diameter of the tubes, with 1.2 nm spatial resolution. In addition, TEM bright field imaging had the spatial resolution to reveal variations in the spacing of layers across the tube diameters, which varied from 2.5 to 4 nm. In another study, Morales *et al.*[43] combined STEM-EELS and (hard X-ray) bulk XAS measurements to determine the location and electronic state of the Mn promoter in cobalt Fischer–Tropsch catalysts. STEM-EELS was used to determine the elemental distribution of Mn relative to the nanoparticulate Co catalysts, while hard X-ray XAS was used to study the Mn K edge, which is not accessible in EELS due to its high energy position at ~6540 eV. Analysis of both the near-edge and extended fine structure at the Mn K edge allowed Morales *et al.* to differentiate between MnO_2 and Mn substituted into the spinel structure in differently prepared samples. These examples demonstrate that combining high

Nanoscale Accepted Manuscript

This journal is © The Royal Society of Chemistry [year]

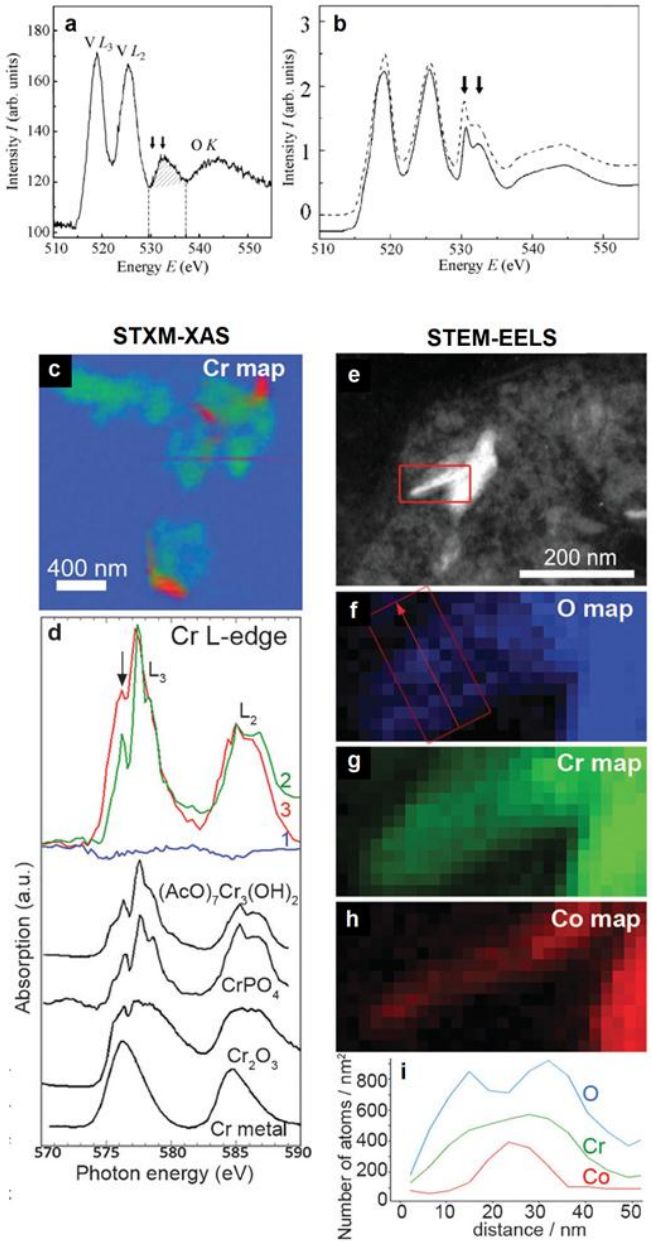

Fig. 4 Correlative XAS-EELS studies. (a) EEL spectrum from a 1.2 nm spot of a single V_2O_5 nanotube showing an asymmetry in a feature at the oxygen K edge (shaded). (b) Bulk XAS spectrum of the same sample (solid line) and a bulk V_2O_5 reference (dashed line) displaying additional fine structure at the oxygen K edge (arrows).Reprinted with permission from Gloskovskii *et al.*[39] Copyright 2007, AIP Publishing LLC. (c-d) STXM-XAS chemical analysis of the speciation of Cr in CoCrMo wear particles, compared to (e-i) elemental maps across individual nanoparticles from the same sample acquired by STEM-EELS. Reproduced from reference 40.

resolution STEM-EELS with spatially-averaged XAS is a powerful approach which can provide a more complete characterisation of the structure and chemistry of nanoscale systems.

The addition of STXM-XAS to a correlative study of CoCrMo nanoparticles from metal-on-metal hip prostheses[40] allowed oxidised and metallic Co signatures to be spatially resolved,

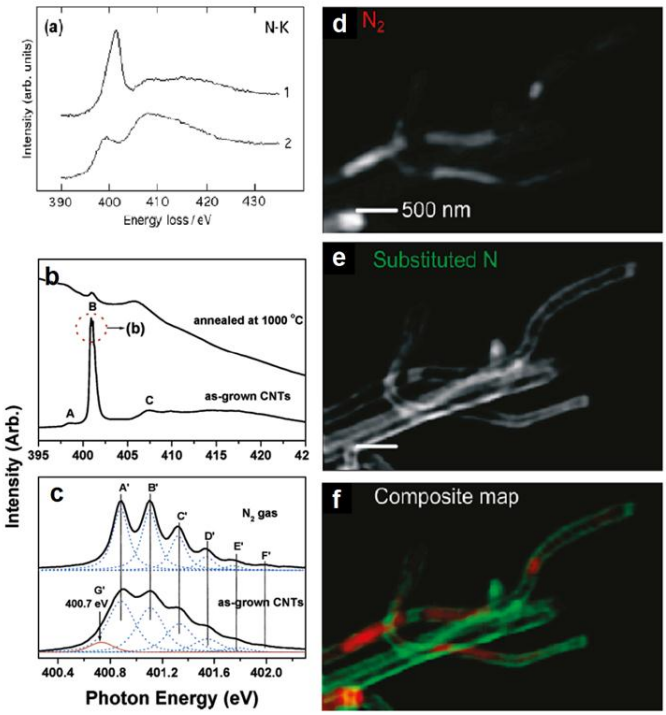

Fig. 5 Comparison of XAS and EELS studies of N-CNTs. (a) EEL spectra from N-CNT before and after electron beam damage, showing a reduction in the peak at 401 eV from molecular N_2.Reproduced from reference 44. (b-c) Area-averaged Nitrogen K edge XAS spectra of N-CNTs before and after annealing. Due to the higher spectral resolution of XAS compared to EELS, the peak at 401 eV can be deconvoluted into seven peaks, which is indicative of vibronic structures from gaseous nitrogen. Reprinted with permission from Choi *et al.*[46] Copyright 2005 American Chemical Society. (d-f) Chemical maps showing the location of molecular (red) and substituted (green) nitrogen in N-CNTs obtained by STXM-XAS. Reprinted with permission from Zhou *et al.*[45] Copyright 2010 American Chemical Society.

showing that they arose from distinct wear particles (figure 4 c-i). Improved spatial resolution from STEM-EELS measurements allowed the elemental distribution to be determined across individual nanoparticles, and evidence of a core-shell structure in which metallic particles were surrounded by an oxygen-rich, cobalt-depleted layer was observed.

To explore how the addition of spatially-resolved XAS measurements can further benefit nanoscale characterisation, we consider a number of studies on nitrogen-doped carbon nanotube (N-CNT) systems. Nitrogen doping is performed either to tailor electrical properties of the CNTs themselves, or as a means of storing nitrogen gas.[44, 45] In order to assess the suitability of N-CNTs for these applications and to understand the doping process, it is important to be able to distinguish between the different chemical forms of the nitrogen present, and to map their distributions across individual N-CNTs.

The first study to report N_2 gas within N-CNTs employed STEM-EELS.[44] In this work, a peak at 401 eV was observed, corresponding to gaseous N_2 (figure 5a). This peak disappeared after exposure to the electron probe, due to the creation of holes in the graphitic tube walls and subsequent release of the N_2 gas. EEL spectra acquired from damaged regions, where gaseous N_2 had escaped, were consistent with nitrogen incorporated into the sp^2 carbon network of the nanotube walls. A later study by Choi

Nanoscale Accepted Manuscript

et al.[46] employed XAS as well as EFTEM elemental mapping to characterise N-CNTs. XAS at the N K edge demonstrated the presence of pyridine-like and graphite-like nitrogen in the N-CNTs, as well as the peak at 401 eV consistent with the previous EELS study. However, due to the higher spectral resolution of XAS compared to EELS, Choi *et al.* were even able to resolve the vibronic structures within the gaseous N_2 peak (figure 5b,c). As the XAS measurements were not spatially resolved however, EFTEM elemental mapping was also performed. EFTEM maps revealed that nitrogen was located in the hollow of the N-CNTs.

Using STXM, it is now also possible to obtain spatially resolved XAS across *individual* N-CNTs. Zhou *et al.*[45] demonstrated the capabilities of STXM in mapping different nitrogen species across N-CNTs without resorting to EELS (figure 5 d-f). STXM maps provided direct confirmation that substituted nitrogen is located in the nanotube walls and molecular nitrogen is trapped within nanotube compartments. The surface-sensitivity of the TEY detection mode was even exploited to obtain spectra from substituted nitrogen alone, without the large signal from molecular nitrogen. Furthermore, the intensity of the nitrogen signal was used to estimate the pressure within N-CNTs as being ~50 atm, and the broadening of the vibrational features on the 401 eV peak was used to support the conclusion of such a high N_2 pressure.

As the spatial resolution of the STXM in this study was 30 nm, the success of the detailed analyses was due in part to the relatively large diameters of the N-CNTs studied (>200 nm). To investigate narrower nanotubes, or other features smaller than ~30 nm, electron microscopy techniques are still required. For example, EFTEM tomography has been used to map the distribution of nitrogen throughout a 40 nm diameter N-CNT,[47] and at an even higher resolution, recent work by Arenal *et al.*[48] demonstrated the capabilities of STEM-EELS in identifying individual N dopant atoms in a single-walled CNT.

Spectroscopy under realistic conditions

Both electrons and soft X-rays interact strongly with matter. The transmission requirement poses strict limitations on both the thickness of samples (often ultrathin sections are prepared from solid samples) as well as the environment they are in. STXMs may operate at pressures ranging from 1 to 10^{-9} bar,[49] while TEMs require high vacuum conditions of 10^{-10} bar or lower[2] to minimise beam interactions with gases. However, many chemical processes occur at gas-solid or liquid-solid interfaces, far from the environment within X-ray and electron microscopes. To allow samples to be studied under conditions more closely resembling their native state, nanoreactors have been developed which can confine gases or liquids within layers thin enough to be transparent to the electron/X-ray beam. An alternative scheme for environmental studies in the TEM is a differentially pumped vacuum system, in which the sample chamber is separated from the rest of the column by apertures and kept at a higher pressure, on the order of 50 mbar.[50] *In situ* microscopy techniques provide different opportunities and pose different challenges within electron and X-ray microscopes. To illustrate this, selected applications of environmental spectro-microscopy will be considered in the following case studies.

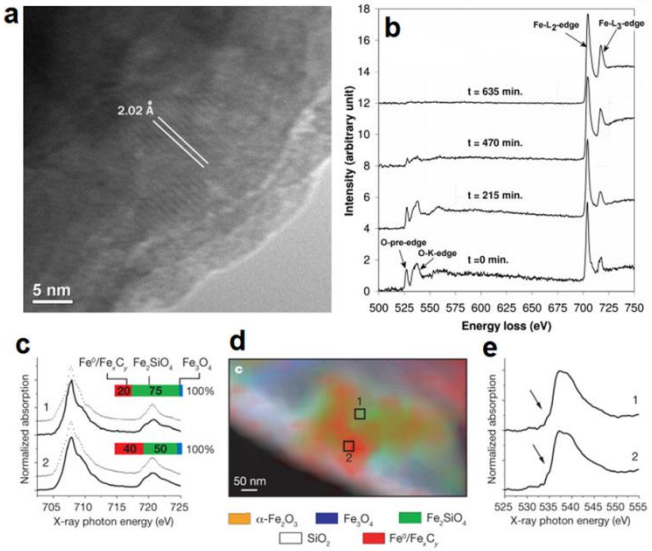

Fig. 6 (a) High resolution TEM micrograph of FT catalyst which was carburised at 20 Torr CO *in situ* using a differentially pumped TEM. The pressure was lowered to < 3.5 Torr during imaging. Lattice spacings consistent with α-Fe are marked. EELS from the same study showing the evolution of oxygen and iron edges. Iron Fe L_3/L_2 ratios and elemental Fe/O ratios are also consistent with the presence of metallic Fe. Reprinted from 52 with permission from Elsevier. (d) Chemical map of a Fe-based catalyst collected *in situ* by STXM after 4 h in synthesis gas at 250 °C. Fine structure in the Fe $_{L2,3}$ (c) and oxygen K edge (e) were used to determine relative contributions of different iron phases in regions labelled 1 and 2. Reprinted by permission from Macmillan Publishers Ltd:Nature[53] copyright 2008.

Gas cells and Fischer-Tropsch catalysts

Fischer-Tropsch (FT) synthesis involves the conversion of CO and H_2 (syngas) into hydrocarbons for use as synthetic fuels and oils. Industrial iron-based FT catalysts are mainly composed of iron oxide on silicon dioxide. In this complex iron-oxygen-carbon system, questions remain about the identity of the active phase responsible for catalysing the reaction. As the FT reaction occurs at high temperatures and pressures, conventional electron microscopy analysis of the catalyst can only be carried out on catalysts before and after the reaction. Such *ex situ* experiments are difficult to perform in these samples as they are highly air-sensitive. To overcome this, Janbroers *et al.* used a protective atmosphere sample holder to transfer catalyst samples from the reactor into the electron microscope.[51] TEM-EEL spectra of these quasi-*in situ* samples yielded significantly different results to previous studies: iron carbides were observed in the activated catalyst; a phase which would have been re-oxidised on exposure to air using conventional transfer protocols.

However, the above approach does not address the fundamental issue when investigating any dynamic process like catalytic activity: the state of the catalyst *after* activation may not accurately reflect its state *during* the reaction.[54] As functionally-relevant active phases might only form under reaction conditions, environmental methods are needed to study the evolution of the system *in situ*, whilst the reaction is occurring. A subsequent study by Janbroers *et al.*[52] used a differentially pumped TEM to acquire atomic-resolution images and EEL spectra of an iron-based FT catalyst during activation. Due to the considerable engineering challenge of confining a gas environment around the

Nanoscale Accepted Manuscript

This journal is © The Royal Society of Chemistry [year]

sample whilst maintaining high-vacuum conditions in the rest of the microscope, the maximum pressure obtainable during the *in situ* carburisation reaction was < 0.1 bar, two orders of magnitude lower than normal working conditions. Additionally, as multiple scattering events deteriorate both the spatial resolution of TEM imaging and the visibility of EELS edges, this pressure had to be further reduced to 5×10^{-3} bar during TEM and EELS acquisition. Within these limitations, the authors observed the evolving reduction of the iron oxide precursors during CO treatment at 270 °C. The low Fe L_3/L_2 ratio combined with a high Fe/O ratio suggested that metallic iron was present along with iron carbides. This was further supported by TEM analysis, which had sufficient spatial resolution to image lattice spacings consistent with α-Fe (figure 6a,b).

Nanoreactors may be used to achieve even higher pressures *in situ* compared to a differentially pumped TEM. De Smit *et al*.[55] performed an STXM study of FT catalysts under pressures of 1 bar, achieved by containing the catalyst and gas between two 1.2 μm thick SiN_x membranes. A Pt resistive heater was used to provide temperatures of up to 500 °C. This work examined the catalysts during activation in H_2, as well as during FT synthesis (figure 6 c-e). XAS at the Fe $L_{2,3}$ and O K edges were used to determine chemical and spatial alterations of different iron species (metal, oxides and carbides) at each step. The spectra obtained were similar to the EELS measurements discussed above, but with high enough spectral resolution to resolve crystal field effects, revealing that the iron was in an octahedral coordination, probably as Fe_2SiO_4. In addition to this, changes in the fine structure at the C K edge allowed different carbon species to be identified as either iron carbides or reaction products. Once again this analysis was limited by the 15 nm spatial resolution of the STXM. As this is the same size as many iron oxide crystallites which make up the catalyst,[52] STXM alone has insufficient spatial resolution to probe compositional variations within individual catalyst nanoparticles. However, the nanoreactor used in this study was originally designed for the electron microscope,[56] and future *in situ* EELS studies may be able to provide complimentary information on a finer length scale.

Hydrated states

Many systems are hydrated in their native state, and these have also benefited from the introduction of nanoreactors which allow controlled humidity, keeping samples hydrated throughout the experiment. TEMs and STXMs have been used to study a range of processes in liquids such as nanoparticle growth,[57] corrosion[58] and electrochemical processes (*e.g.* lithiation/delithiation of battery anodes).[59] In the TEM, the majority of studies in liquids have been performed in imaging modes rather than spectroscopy. This is due in part to the shadowing of EDX detectors by liquid cell holders, however modified liquid cell holders have very recently been developed,[60] and in a test sample EDX maps were acquired from Au nanoparticles in 150 nm of liquid with 30 nm spatial resolution. EELS measurements do not suffer the same geometrical constraints as EDX, but are once again limited by multiple scattering events which greatly reduce the signal to background ratio. It has been suggested that while core-loss EELS measurements are only practical through < 3 inelastic mean free paths (which corresponds to a 300 nm cell thickness at 200 keV), valence-loss EELS signals at energies below the plasmon peak are less sensitive to thickness effects and may be used to provide chemical information of samples up to six inelastic mean free paths (or 600-700 nm at 200 keV) in thickness.[61] For comparison, the relaxed thickness constraint for valence-loss EELS is still an order of magnitude smaller than acceptable wet-cell dimensions for soft X-ray STXM,[8] not to mention the larger path lengths which may be probed by extending into the hard X-ray regime.

An important consideration in liquid cell experiments is the effect of the probe on the liquid sample. High energy electron beams are known to decompose water, and the radiolytic products which form may trigger undesirable reactions.[62] On the other hand these reactions have been the basis of a number of electron beam-induced nucleation studies.[63, 64] In either case the effect of electron, as well as X-ray dose on *in situ* results must be carefully considered; their effects on reaction kinetics and any structural and chemical beam-induced modifications must be quantified.

One important application for microscopy of hydrated samples is in the field of biology. Conventional preparation for TEM or STXM studies of biological systems involves arresting the cellular processes (fixation) and dehydrating the sample so that it may be compatible with the low pressure environments within the microscope.[65] Heavy metal stains and tags may also be used to provide contrast from components of interest. Although much work has gone into optimising sample fixation and dehydration protocols, they often result in undesirable structural and morphological modifications of the sample, and so avoiding dehydration altogether is a popular route to preserving cellular chemistry and morphology.

There are two main routes available to investigate cells in the hydrated state, namely liquid-cell holders[8, 66] and cryo-methods.[67] In cryo-microscopy, samples are rapidly frozen to induce vitreous ice formation. Vitrified samples then must be maintained below -135 °C during the course of experiments to prevent the formation of ice crystals which would grow, displacing ions and damaging cellular components.[65] STEM-EELS studies carried out on frozen hydrated specimens have revealed the distribution of water and proteins in frozen hydrated sections of rat liver.[68] Vitrified cellular systems are often imaged using soft X-rays (usually in full field TXMs) in the 'water window' i.e. with energies between the carbon and oxygen K edges at 284 and 543eV respectively.[69] Water-window imaging provides good contrast from carbonaceous species without absorption from the surrounding ice. Recently cryo-TXM studies have been correlated with optical microscopy,[70] in which fluorescent tags are used to provide spatially resolved compositional information within live cells on length scales of ~ 1 μm.

The correlation of optical microscopy with electron and X-ray microscopy techniques is an important direction for biological investigations, as this provides the ability to observe processes in live cells at lower spatial resolution using optical techniques, and then investigate a snapshot of that process in fixed cells with much higher spatial resolution. Detailed studies of live cells using soft X-ray or electron microscopy have not been carried out to date and preliminary investigations indicate that radiation damage is a critical issue in unfixed biological samples, leading to

Nanoscale Accepted Manuscript

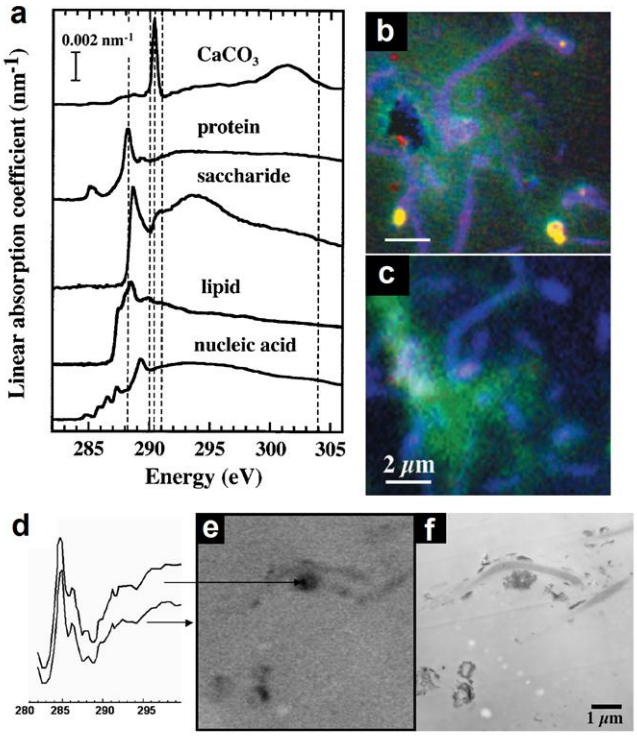

Fig. 7 (a) XAS of different components within biofilm samples, and (b) chemical map derived from STXM image sequences and colour coded to show lipids (red), saccharides (green) and proteins (blue). (c) Confocal fluorescence microscopy maps from the same area were stained with probes for the saccharide fucose (green) and nucleic acids (blue) and show remarkably similar distributions of these components. (d) XAS, (e) X-ray absorption image (f) and TEM micrograph recorded from the same area of a resin-embedded biofilm sample. Spectra from resin and a bacterium are very similar, indicating that embedding did not preserved cell contents well. However the ability to image this sample in the TEM provides highly spatially resolved morphological information.[66] Amended with permission from American Society for Microbiology.

blebbing and cell death after doses as low as 0.4 $e^{-}/Å^{2}$.[71] A number of recent studies on biofilms (communities of bacterial cells, and their surrounding organic matrix) which employ correlative light microscopy, liquid cell and cryo-preparation techniques are reviewed below. These studies demonstrate the advantages of maintaining biological samples in the hydrated state, and show how STXM-XAS may be used to gain more detailed spectroscopic information from hydrated biological samples than the water-window imaging technique.[66, 72]

Dynes *et al.*[73] demonstrated that it is possible to perform correlative optical microscopy, TEM and STXM on a single sample by using an elegant labelling technique. In this work, biofilm sections were labelled with CdSe/ZnS quantum dots designed to bind to polysaccharides. The nanoparticle probes provide contrast in all three microscopes via a) fluorescence in light microscopy b) z-contrast in TEM and c) absorption at the Se, Zn or Cd edges in STXM, allowing the distribution of polysaccharides to be imaged at three different length scales.

Lawrence *et al.*,[66] used a range of fluorescent markers to stain nucleic acids, proteins, lectins and lipids within a river biofilm sample (figure 7). Confocal laser scanning microscopy (CLSM) was then used to map these components across hydrated samples contained in silicon nitride 'wet cells'[74] with spatial resolution of < 1 μm. As well as the limited spatial resolution of this optical microscopy technique, fluorescent staining is indirect and relies on the specificity of the markers to bind to the right cellular component. The tagging reaction is also not fully quantitative as it is affected by dense samples, through which the markers may not be able to penetrate. To enable the quality of fluorescent staining to be assessed, direct measurements of component distributions were acquired using STXM-XAS. Wet cells previously imaged by CLSM were subsequently loaded into a STXM, and the near-edge structure at the carbon K edge was used to differentiate between nucleic acid, proteins and lipid structures. Maps of these components determined from direct XAS measurements were compared with fluorescent images, and the specificity of the fluorescent probes was confirmed.

As the wet cell used in this study was too thick to be electron transparent, biofilm samples were prepared through conventional dehydration and resin-embedding for TEM analysis. Thin sections of resin-embedded biofilms were imaged in the TEM as well as STXM. TEM imaging provided much more detailed morphological information of the cells and extracellular matrix. However, XAS spectra taken from a bacterium cell was very similar to spectra of the embedding resin, suggesting that resin-embedding had failed to preserve the organic material within the cells (figure 7 d-f).

In an attempt to preserve cell composition to a greater degree than resin-embedding, a later correlative STXM-TEM study by Hunter *et al*. used freeze-dried cryo-sections.[72] Biofilm samples were frozen at high pressure to ensure consistent vitrification, microtomed at liquid nitrogen temperatures, and then gradually warmed up to 25 °C. XAS carbon K edge spectra showed fine structure characteristic of proteins, lipids and polysaccharides within cells, demonstrating that the macromolecular composition of cells had been better preserved through freeze-drying. Additionally, the absence of resin and its associated absorptions at the carbon K edge allowed the biological macromolecules to be more easily identified. TEM imaging once again revealed morphological structure, and XAS spectra this time revealed protein signals in the bacteria. However, lower than expected lipid and polysaccharide signals were observed, indicating some movement of organic matter had occurred during this sample preparation.

Damage studies

Many of the most successful correlative electron/X-ray spectroscopy studies have been carried out on inorganic systems. In the biofilm studies discussed above, the detailed spectroscopic information was obtained using soft X-rays only, and the TEM was limited to imaging sample morphology. It is interesting to ask if STEM-EELS would have sufficient chemical sensitivity to distinguish between cellular components at the carbon K edge, as was possible in the STXM. To answer this question we must consider the effects of radiation damage. In carbon systems, it is often assumed that EELS is the more damaging of the two techniques, however it is still unclear to what degree this is true, and direct comparisons of damage are few and far between. Such comparisons are difficult because the mechanisms of damage are complex and not completely understood. Also, relevant

Nanoscale Accepted Manuscript

This journal is © The Royal Society of Chemistry [year]

Cite this: DOI: 10.1039/c0xx00000x

www.rsc.org/xxxxxx

ARTICLE TYPE

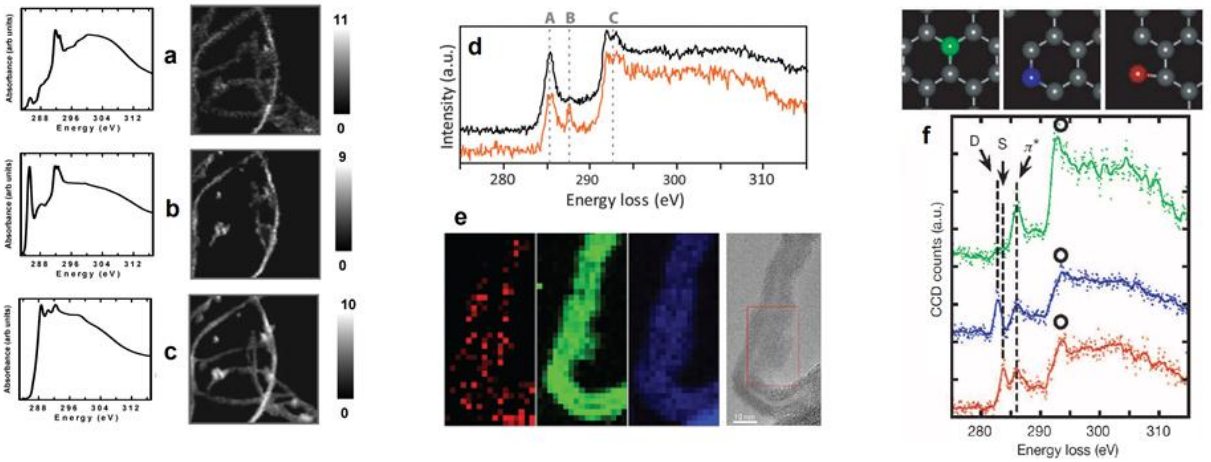

Fig. 8 Examples of studies of carbon K edge fine structure using XAS and EELS. STXM-XAS spectra and maps of chemical components present in dodecyl-functionalised SWNTs: horizontal SWNTs (a), vertical SWNTs (b) and dodecyl (c).Adapted with permission from Najafi *et al.*[77] Copyright 2010 American Chemical Society. (d) EEL spectra at the carbon K edge for pristine (black) and oxidised (orange) MWNTs. (e) From EELS spectrum images, the spatial distributions of the oxidised peak B (red), graphitic carbon signal (green) and amorphous carbon (blue) were extracted and compared with high resolution TEM images of the same MWNT. Reproduced from Ref. 78. (f) Monochromated EEL spectra taken from the coloured edge atoms show different fine structure due to the different coordination environments.Reprinted by permission from Macmillan Publishers Ltd:Nature,[79] copyright 2010.

parameters such as probe brightness and diameter are constantly changing as instruments improve. A widely cited study by Braun *et al.*[76] comparing EELS and XAS was carried out on particles of diesel soot. In this study the electron beam was defocused to 100 nm to reduce the dose, however EEL spectra still showed only π* and σ* features with no fine structure and no variation between different particles. In contrast, XAS spectra contained multiple peaks between 285 and 290 eV, indicative of the presence of carbonyl and carboxyl groups. While it is probable that electron beam damage contributed greatly to the differences between the EELS and XAS spectra, the effects of a) the different sample preparation routes used and b) the different energy resolutions of EELS and XAS, also need to be quantified. This study illustrates the importance for experimenters to state the dose, in electrons (or photons) per square nanometer, to enable different experiments to be compared. Another correlative STXM/EELS study by Alexander *et al.*[75] on similar carbonaceous airborne particles also found that EEL spectra lacked features characteristic of functional groups. However they observed that the use of STXM alone misses important morphological and structural information, and so a correlative approach was suggested, in which STXM is first used for chemical analysis and subsequent TEM imaging is used to analyse particle morphology.

More quantitative studies have investigated damage rates on poly(ethylene terephthalate) (PET), comparing 100 keV electrons with soft X-rays at the carbon and oxygen K edges.[80] Through analysis of the near edge structures, the damage products were found to be the same. They also found that the critical dose for PET was an order of magnitude higher for X-rays than for electrons. However, this study has been criticized on a number of points, including a) the use of a 100 keV electron beam which is above the threshold for knock-on damage of carbon,[81] thereby introducing an additional damage mechanism which is not present in X-ray spectroscopy, and b) the use of different microscopes to evaluate the critical dose, i.e. the TEM was used to evaluate electron damage while the STXM was used to evaluate X-ray damage.[8, 82] These points were addressed in a subsequent study[82] in which a) a lower energy electron beam of 80 keV minimised knock-on damage, and b) the spectral evaluation of both electron and X-ray damage was performed in the STXM. PET samples were exposed to a range of doses and afterwards XAS spectra were taken of the series of spots. Using this method PET was found to display similar damage chemistries for *both* electrons and X-rays, with similar critical doses of 4.2×10^8 Gy. As there are considerable differences between the primary processes of electron and X-ray irradiation, this result indicates that secondary processes (the generation of low energy secondary electrons and ions in both electron and X-ray cases) govern radiation damage. In the remainder of this section we consider a number of studies employing electron and X-ray spectroscopy to characterise carbon-based systems with a range of radiation-sensitivities, from relatively stable graphitic nanoparticles to beam-sensitive organic samples.

Carbon K edge

Both STXM-XAS and STEM-EELS have been used to obtain fine structure at the carbon K edge in graphitic nanomaterials such as graphene,[23, 83] carbon nanotubes[84, 85] and C_{60}.[86, 87] As well as characterising graphitic nanoparticles in their pristine states, it is useful to determine the distribution of any functional moities on the nanomaterial surfaces as knowledge of the distribution of groups would facilitate better understanding of the

Nanoscale Accepted Manuscript

Cite this: DOI: 10.1039/c0xx00000x

www.rsc.org/xxxxxx

ARTICLE TYPE

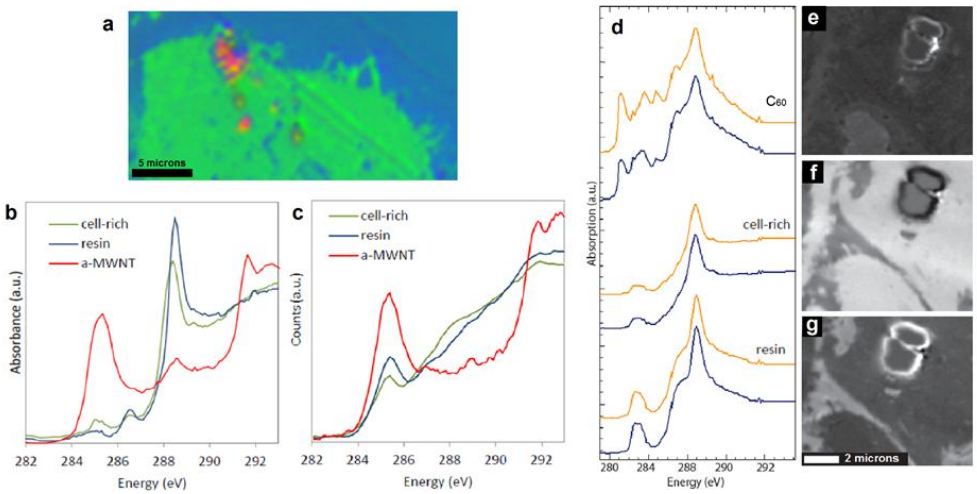

Fig. 9 Correlative XAS and EELS of carbon nanomaterials within biological cells. (a) STXM-XAS chemical map and (b) corresponding spectra of multi-walled carbon nanotube aggregates in a cell, with resin displayed in blue, cell-rich areas in green and carbon nanotubes in red. (c) STEM-EEL spectra of the same sample show significant damage to the resin and cell components compared to XAS results. Clusters of C_{60} were also mapped within cells using STXM-XAS. (d) XAS spectra and (e-g) maps showing the distribution of C_{60}, cell and resin respectively within the thin sample. Data acquired at beamline X1A1 of the National Synchrotron Light Source, Brookhaven National Laboratory.

functionalisation processes. Najafi *et al.*[77] recently demonstrated that STXM-XAS is able to distinguish between the very similar carbon K edge fine structure of a) graphitic carbon, b) oxidised single-walled carbon nanotubes (SWNTs), c) carbon contaminants and d) dodecyl in samples of SWNTs functionalised with dodecyl groups (figure 8 a-c). This was the first report of direct, spatially resolved characterisation of functional groups on the surface of carbon nanotubes. However, when trying to map the contributions of each chemical component over SWNT bundles, some errors were observed due to the similarities between spectra from different components, illustrating that even with the high chemical sensitivity of XAS techniques, distinguishing between functionalised and pristine carbon signals is non-trivial. A similar study by Goode *et al.*[78] used 80 kV STEM-EELS to investigate the electronic structure of oxidised multi-walled carbon nanotubes (MWNTs). A peak at 287.2 eV was observed in the carbon K edge which is consistent with oxygen-containing defect structures, and was mapped across individual MWNTs (figure 8 d,e). Although the spatial resolution in this EELS study was limited by electron beam damage to 5 nm, this is a factor of six better than STXM measurements of the dodecyl-SWNT system. Electron beam damage to edge and surface states may be reduced by further lowering the energy of the electron beam. Using an operating voltage of 60 kV, Suenaga *et al.*[79] performed STEM-EELS measurements across the edge of graphene sheets. The combination of low operating voltage and an aberration-corrected electron probe allowed atom-by-atom measurements at graphene edges, and revealed a new peaks at 282.6 ± 0.2 eV 283.6 ± 0.2 eV corresponding to edge atoms doubly or singly bonded at the edge (figure 8f).

The graphitic nanomaterials described above have attracted much interest due to their unique chemical and physical properties, and their potential applications range from optical and electronic materials to drug delivery vehicles. To assess the feasibility of carbon nanomaterials in biological applications, and to understand the effects of environmental exposures from engineering applications, it is important to be able to determine the fate of these nanomaterials in the cellular environment. Both electron and X-ray spectroscopy techniques can provide insights into nanoparticle-cell interactions. Figure 9 shows STXM-XAS and STEM-EELS analysis of human monocyte-derived macrophage cells two weeks after internalising multi-walled carbon nanotubes. Both XA and EEL spectra acquired over MWNT clusters contained peaks at 285 and 292 eV characteristic of graphitic carbon, demonstrating that the structure of the MWNTs had not been fully degraded after two weeks. Graphitic spectra are distinct from the rest of the resin-embedded cell section, allowing the MWNT clusters to be easily mapped using either technique. However while XAS spectra displayed obvious differences between the areas which contain cell compared to areas containing only resin, EEL spectra of these two components are lacking in fine structure and difficult to tell apart. It is likely that electron beam damage contributed to the differences between XAS and EEL spectra of resin and cells.

Figure 9 (d-g) displays our unpublished data showing the capability of STXM-XAS for mapping core-loss transitions in the related system of C_{60} in macrophage cells. To achieve mapping of the C_{60}/cell interface with higher spatial resolutions in the transmission electron microscope, Porter *et al* [88] made use of low-loss transitions instead. These transitions have much larger cross sections than excitations of core states, allowing shorter acquisition times, and lower doses. Therefore making use of the

Nanoscale Accepted Manuscript

Cite this: DOI: 10.1039/c0xx00000x

www.rsc.org/xxxxxx

ARTICLE TYPE

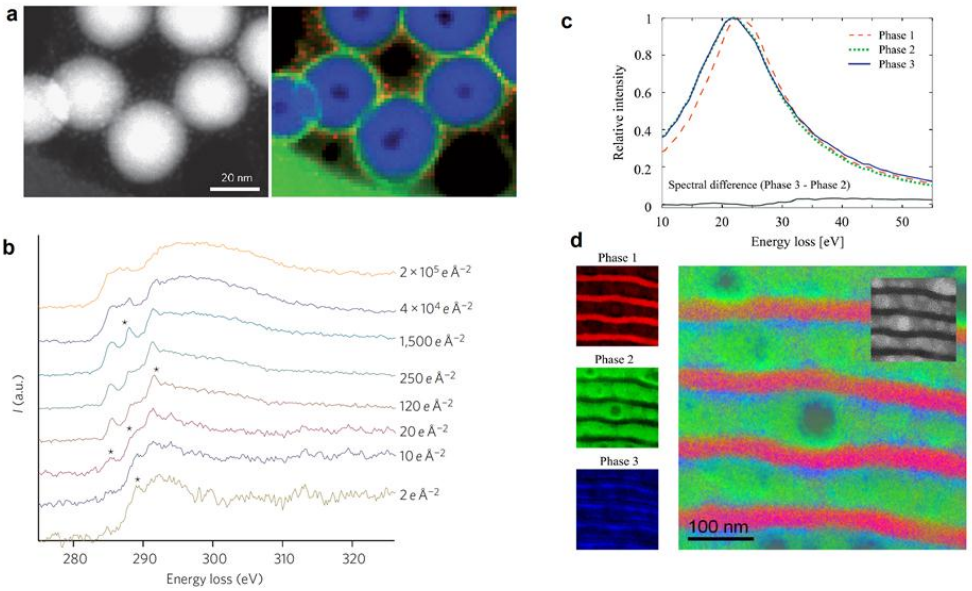

Fig. 10 Comparison of core-loss and valence-loss EELS of organic materials. (a) HAADF image of the organic-inorganic nanoparticles and composite colour map showing elemental distributions of gadolinium (red), silicon (blue) and carbon (green). Reprinted by permission from Macmillan Publishers Ltd:Nature,[89] copyright 2010. (b) EEL spectra of the octadecane and lipid layer from the same study as a function of electron dose. Degradation of the organic layer is observed which clearly alter the fine structure of the carbon K edge. amorphous carbon. (c) Three similar but distinct plasmon peak signatures were obtained from PCA-processed valence-loss spectrum images of a PS-b-PEO block co-polymer sample. (d) The phases were mapped across the sample, with colours corresponding to spectra in (c).Reprinted from Ref. 90 with permission from Elsevier.

low loss region of EEL spectra is a powerful strategy for studying radiation sensitive samples. In this study Porter *et al.* demonstrated that the shift in π + σ plasmon peak between 22 and 26 eV could be used to distinguish between C_{60} and cellular carbon, and thus mapped the distribution of C_{60} crystals within the cells.

Recently van Schooneveld *et al.*[89] have used STEM-EELS to characterise hybrid organic-inorganic nanoparticles. The nanoparticles were composed of a Cd-containing quantum dot core surrounded by a silica shell, and coated with octadecane and two lipids: a PEG lipid and a Gd-containing lipid. High angle annular dark field (HAADF) imaging was used to reveal the morphology of the nanoparticles at different stages of their synthesis, and EELS data provided impressive quantification of the inorganic component in the form of elemental maps of Cd, C, Si, Gd (figure 10a). EELS measurements of the organic layer, however, were more difficult. The electron dose required to perform sub-nanometre EELS with adequate SNR was found to degrade the lipids, altering the near edge structure at the carbon K edge (figure 10b). However, small differences in the fine structure were observed between amorphous carbon and damaged lipid spectra. To avoid the damage associated with EELS, the authors instead used lower dose HAADF imaging to characterise the organic layer. Using atomic number contrast in HAADF images, which made the Gd atoms appear brighter, the PEG:Gd-lipid ratio could be estimated.

Low-loss EELS and statistical methods

Allen *et al.*[90] have achieved more success mapping PEG-related species using low-loss EELS. Spatially resolved plasmon peak information was recorded for a block co-polymer electrolyte consisting of poly (styrene-block-ethylene oxide) (PS-b-PEO). Low-loss EFTEM spectrum images were collected with reduced electron doses, and analysed by principal component analysis (PCA) to create component maps (figure 10c,d). Studies such as this in the valence loss region of EEL spectra can be challenging to interpret, as relatively few first-principle calculations have been performed to assist interpretation compared to the core-loss EELS. Without *a priori* knowledge of the spectral components in a complex sample, PCA and other related multivariate statistical analysis (MSA) routines can be invaluable for analysis of the datasets. PCA analyses a dataset as a whole, and identifies the significant variations within the dataset. Variations are described by 'principal components', which can be thought of as *abstract* EEL spectra. As well as subtle variations in plasmon peaks and valence-loss EEL spectra, PCA has been used to map variations in bonding using core-loss EELS fine structure.[91] As principal components can be ordered by the magnitude of the variations they describe, low-magnitude variations can be discarded as noise. In this way, PCA can also achieve noise filtering without loss of spectral resolution. Noise filtered datasets may be further used for efficient semi-automated processing, such as cluster analysis.[92] PCA and cluster analysis can reveal subtle changes in

Nanoscale Accepted Manuscript

large datasets which may otherwise be overlooked by manual inspection.[93] Details about PCA and its application to EELS and XAS can be found elsewhere.[92-94]

The examples discussed above demonstrate that STXM-XAS is capable of providing detailed spectral information of organic carbon species, whilst obtaining fine structure in EEL spectra of the same materials remains challenging due to electron beam damage. However, there are a number of recent studies which show that in state-of-the-art electron microscopes, with optimised conditions, it is possible to distinguish between selected carbon species using differences in core-loss EELS fine structure, even with atomic-scale resolution. This situation can be expected to improve as detector efficiencies improve (and with furthered understanding of damage mechanisms, allowing optimal acquisition conditions to be chosen). Alternatively, the use of lower-dose valence-loss EELS to characterise beam-sensitive samples has been demonstrated to be a successful strategy. Advanced statistical analysis of datasets can also facilitate lower dose measurements as they enable spectra with lower signal-to-noise ratios to be analysed. In X-ray microscopy, improvements in spatial resolution can be expected both through advanced fabrication of X-ray optics, as well as a shift towards diffraction-based techniques such as ptychography.

Conclusions

The combination of these two independent, complementary techniques to probe electronic structure is invaluable. In systems which do not require the highest spatial or spectral resolutions, where the experimental question is regarding changes in chemistry which occur on length scales greater than X-ray probe diameter and where electron and X-ray damage is negligible, the information obtained from EELS and XAS is equivalent and allows cross-validation of findings.

For systems where the required spatial and/or energy resolution cannot be met by STEM-EELS or STXM-XAS alone, (*e.g.* investigations of interfaces or multiplet splittings in transition metals) correlation of the two techniques becomes essential for bridging the spatial and spectral gaps.

Even for biological or polymer samples which are challenging to characterise using EELS due to electron beam damage, correlations between STXM-XAS chemical maps and TEM imaging can greatly assist understanding. Extensions to techniques such as low-loss EELS, surface sensitive XAS detection methods, hard X-ray spectroscopies or optical microscopy provide the opportunity to probe different facets of a system, making the correlative micro-spectroscopy approach a powerful and flexible tool for the materials scientist.

Acknowledgements

We thank Sue Wirick for assistance during synchrotron beamtime. Funding was provided by EPSRC Science and Innovation Programme: EP/D063329, an EPSRC Doctoral Prize Fellowship (AEG) and ERC starting investigator grant #257182 (AEP).

Notes and references

[a] *Department of Materials, Imperial College London, London SW7 2AZ, UK, Email: aeg08@ic.ac.uk*
[b] *Department of Materials Science and Engineering, The Ohio State University, Columbus, Ohio 43210, USA. Email: mccomb.29@osu.edu*

1. P. M. Bertsch and D. B. Hunter, *Chemical Reviews*, 2001, **101**, 1809-1842.
2. D. B. Williams and C. B. Carter, Plenum Publishing Corporation, New York, 1949.
3. M. A. Aronova and R. D. Leapman, *MRS Bulletin*, 2012, **37**, 53-62.
4. R. F. Egerton, *Reports on Progress in Physics*, 2009, **72**.
5. H. Ade, A. P. Smith, H. Zhang, G. R. Zhuang, J. Kirz, E. Rightor and A. Hitchcock, *Journal of Electron Spectroscopy and Related Phenomena*, 1997, **84**, 53-71.
6. T. R. Neu, B. Manz, F. Volke, J. J. Dynes, A. P. Hitchcock and J. R. Lawrence, *Fems Microbiol Ecol*, 2010, **72**, 1-21.
7. F. M. F. de Groot, E. de Smit, M. M. van Schooneveld, L. R. Aramburo and B. M. Weckhuysen, *Chemphyschem*, 2010, **11**, 951-962.
8. A. P. Hitchcock, J. J. Dynes, G. Johansson, J. Wang and G. Botton, *Micron*, 2008, **39**, 741-748.
9. J. C. Andrews, F. Meirer, Y. J. Liu, Z. Mester and P. Pianetta, *Microsc. Res. Tech.*, 2011, **74**, 671-681.
10. P. Fischer, T. Eimuller, G. Schutz, G. Bayreuther, S. Tsunashima, N. Takagi, G. Denbeaux and D. Attwood, *Journal of Synchrotron Radiation*, 2001, **8**, 325-327.
11. B. M. Haines, S. Behyan, S. L. Christensen, M. Obst, D. Bertwistle, C. Karunakaran, T. Tyliszczak and S. G. Urquhart, Canadian Light Source 2008 Activity Report, 2008.
12. D. Vlachos, A. J. Craven and D. W. McComb, *Journal of Physics-Condensed Matter*, 2001, **13**, 10799-10809.
13. T. Walther, H. Stegmann, M. Luysberg, K. Tillmann and T. Weirich, Springer Berlin Heidelberg, 2008, pp. 65-66.
14. G. Margaritondo, *Introduction to synchrotron radiation*, Oxford University Press, 1988.
15. T. Warwick, H. Ade, A. P. Hitchcock, H. Padmore, E. G. Rightor and B. P. Tonner, *Journal of Electron Spectroscopy and Related Phenomena*, 1997, **84**, 85-98.
16. K. V. Kaznatcheev, C. Karunakaran, U. D. Lanke, S. G. Urquhart, M. Obst and A. P. Hitchcock, *Nuclear Instruments & Methods in Physics Research Section a-Accelerators Spectrometers Detectors and Associated Equipment*, 2007, **582**, 96-99.
17. J. Kirz, B. Winn, H. Ade, C. Buckley, M. Feser, M. Howells, S. Hulbert, C. Jacobsen, K. Kaznacheyev, A. Osanna, J. Maser, I. McNulty, J. Miao, T. Oversluizen, S. Spector, B. Sullivan, Y. Wang, S. Wirick and H. Zhang, *Journal of Synchrotron Radiation*, 2000, **7**, 395-404.
18. M. O. Krause and J. H. Oliver, *Journal of Physical and Chemical Reference Data*, 1979, **8**, 329-338.
19. G. Meitzner, *Catalysis Today*, 1998, **39**, 281-291.
20. R. F. Egerton, *Electron energy-loss spectroscopy in the electron microscope*, Plenum Press, New York, 1986.
21. P. J. Goodhew, J. Humphreys and R. Beanland, Taylor & Francis, Inc., London, 2000.
22. K. Suenaga, T. Tence, C. Mory, C. Colliex, H. Kato, T. Okazaki, H. Shinohara, K. Hirahara, S. Bandow and S. Iijima, *Science*, 2000, **290**, 2280-+.
23. Q. M. Ramasse, C. R. Seabourne, D. M. Kepaptsoglou, R. Zan, U. Bangert and A. J. Scott, *Nano Lett*, 2013, **13**, 4989-4995.
24. M. Terauchi, M. Tanaka, K. Tsuno and M. Ishida, *Journal of Microscopy-Oxford*, 1999, **194**, 203-209.
25. R. F. Egerton, *Ultramicroscopy*, 2007, **107**, 575-586.
26. D. S. Su, H. W. Zandbergen, P. C. Tiemeijer, G. Kothleitner, M. Havecker, C. Hebert, A. Knop-Gericke, B. H. Freitag, F. Hofer and R. Schlogl, *Micron*, 2003, **34**, 235-238.
27. O. L. Krivanek, T. C. Lovejoy, M. F. Murfitt, G. Skone, P. E. Batson and N. Dellby, *Journal of Physics: Conference Series*, 2014, **522**, 012023.
28. R. F. Egerton, *Microscopy and Microanalysis*, 2014, **20**, 658-663.
29. P. E. Batson, *Ultramicroscopy*, 1999, **78**, 33-42.

Nanoscale Accepted Manuscript

This journal is © The Royal Society of Chemistry [year]

30. D. A. Muller, L. F. Kourkoutis, M. Murfitt, J. H. Song, H. Y. Hwang, J. Silcox, N. Dellby and O. L. Krivanek, *Science*, 2008, **319**, 1073-1076.
31. K. Kimoto, T. Asaka, T. Nagai, M. Saito, Y. Matsui and K. Ishizuka, *Nature*, 2007, **450**, 702-704.
32. P. E. Batson, *Nature*, 1993, **366**, 727-728.
33. A. B. Shah, Q. M. Ramasse, J. G. Wen, A. Bhattacharya and J. M. Zuo, *Micron*, 2011, **42**, 539-546.
34. W. Chao, P. Fischer, T. Tyliszczak, S. Rekawa, E. Anderson and P. Naulleau, *Opt Express*, 2012, **20**, 7.
35. J. Vila-Comamala, K. Jefimovs, J. Raabe, T. Pilvi, R. H. Fink, M. Senoner, A. Maassdorf, M. Ritala and C. David, *Ultramicroscopy*, 2009, **109**, 1360-1364.
36. D. A. Shapiro, Y.-S. Yu, T. Tyliszczak, J. Cabana, R. Celestre, W. Chao, K. Kaznatcheev, A. L. D. Kilcoyne, F. Maia, S. Marchesini, Y. S. Meng, T. Warwick, L. L. Yang and H. A. Padmore, *Nat Photon*, 2014, **8**, 765-769.
37. Y. Acremann, J. P. Strachan, V. Chembrolu, S. D. Andrews, T. Tyliszczak, J. A. Katine, M. J. Carey, B. M. Clemens, H. C. Siegmann and J. Stohr, *Physical Review Letters*, 2006, **96**, 4.
38. Z. Gainsforth, A. Butterworth, R. Ogliore, A. Westphal and T. Tyliszczak, *Microscopy and Microanalysis*, 2010, **16**, 922-923.
39. A. Gloskovskii, S. A. Nepijko, G. Schonhense, H. A. Therese, A. Reiber, H. C. Kandpal, G. H. Fecher, C. Felser, W. Tremel and M. Klimenkov, *Journal of Applied Physics*, 2007, **101**.
40. A. E. Goode, J. M. Perkins, A. Sandison, C. Karunakaran, H. K. Cheng, D. Wall, J. A. Skinner, A. J. Hart, A. E. Porter, D. W. McComb and M. P. Ryan, *Chemical Communications*, 2012, **48**, 8335-8337.
41. A. P. Hitchcock, T. Tyliszczak, M. Obst, G. Swerhone and J. Lawrence, *Microscopy and Microanalysis*, 2010, **16**, 924-925.
42. A. P. Hitchcock, M. Obst, J. Wang, Y. S. Lu and T. Tyliszczak, *Environmental Science & Technology*, 2012, **46**, 2821-2829.
43. F. Morales, F. M. F. de Groot, P. Glatzel, E. Kleimenov, H. Bluhm, M. Havecker, A. Knop-Gericke and B. M. Weckhuysen, *Journal of Physical Chemistry B*, 2004, **108**, 16201-16207.
44. M. Terrones, R. Kamalakaran, T. Seeger and M. Ruhle, *Chemical Communications*, 2000, 2335-2336.
45. J. G. Zhou, J. A. Wang, H. Liu, M. N. Banis, X. L. Sun and T. K. Sham, *Journal of Physical Chemistry Letters*, 2010, **1**, 1709-1713.
46. H. C. Choi, S. Y. Bae, W. S. Jang, J. Park, H. J. Song, H. J. Shin, H. Jung and J. P. Ahn, *Journal of Physical Chemistry B*, 2005, **109**, 1683-1688.
47. I. Florea, O. Ersen, R. Arenal, D. Ihiawakrim, C. Messaoudi, K. Chizari, I. Janowska and C. Pham-Huu, *Journal of the American Chemical Society*, 2012, **134**, 9672-9680.
48. R. Arenal, K. March, C. P. Ewels, X. Rocquefelte, M. Kociak, A. Loiseau and O. Stephan, arXiv:1401.5007, 2014.
49. J. Raabe, G. Tzvetkov, U. Flechsig, M. Boge, A. Jaggi, B. Sarafimov, M. G. C. Vernooij, T. Huthwelker, H. Ade, D. Kilcoyne, T. Tyliszczak, R. H. Fink and C. Quitmann, *Review of Scientific Instruments*, 2008, **79**.
50. P. L. Gai, E. D. Boyes, S. Helveg, P. L. Hansen, S. Giorgio and C. R. Henry, *Mrs Bulletin*, 2007, **32**, 1044-1050.
51. S. Janbroers, J. N. Louwen, H. W. Zandbergen and P. J. Kooyman, *Journal of Catalysis*, 2009, **268**, 235-242.
52. S. Janbroers, P. A. Crozier, H. W. Zandbergen and P. J. Kooyman, *Applied Catalysis B-Environmental*, 2011, **102**, 521-527.
53. F. M. F. de Groot, E. de Smit, I. Swart, J. F. Creemer, G. H. Hoveling, M. K. Gilles, T. Tyliszczak, P. J. Kooyman, H. W. Zandbergen, C. Morin and B. M. Weckhuysen, *Nature*, 2008, **456**, 222-U239.
54. H. Topsøe, *Journal of Catalysis*, 2003, **216**, 155-164.
55. E. de Smit, I. Swart, J. F. Creemer, G. H. Hoveling, M. K. Gilles, T. Tyliszczak, P. J. Kooyman, H. W. Zandbergen, C. Morin, B. M. Weckhuysen and F. M. F. de Groot, *Nature*, 2008, **456**, 222-U239.
56. J. F. Creemer, S. Helveg, G. H. Hoveling, S. Ullmann, A. M. Molenbroek, P. M. Sarro and H. W. Zandbergen, *Ultramicroscopy*, 2008, **108**, 993-998.
57. L. R. Parent, D. B. Robinson, T. J. Woehl, W. D. Ristenpart, J. E. Evans, N. D. Browning and I. Arslan, *Acs Nano*, 2012, **6**, 3589-3596.
58. S. W. Chee, D. J. Duquette, F. M. Ross and R. Hull, *Microscopy and Microanalysis*, 2014, **20**, 462-468.
59. M. Gu, L. R. Parent, B. L. Mehdi, R. R. Unocic, M. T. McDowell, R. L. Sacci, W. Xu, J. G. Connell, P. H. Xu, P. Abellan, X. L. Chen, Y. H. Zhang, D. E. Perea, J. E. Evans, L. J. Lauhon, J. G. Zhang, J. Liu, N. D. Browning, Y. Cui, I. Arslan and C. M. Wang, *Nano Lett*, 2013, **13**, 6106-6112.
60. N. J. Zaluzec, M. G. Burke, S. J. Haigh and M. A. Kulzick, *Microscopy and Microanalysis*, 2014, **20**, 323-329.
61. M. E. Holtz, Y. C. Yu, J. Gao, H. D. Abruna and D. A. Muller, *Microscopy and Microanalysis*, 2013, **19**, 1027-1035.
62. P. Abellan, T. J. Woehl, L. R. Parent, N. D. Browning, J. E. Evans and I. Arslan, *Chemical Communications*, 2014, **50**, 4873-4880.
63. T. J. Woehl, J. E. Evans, L. Arslan, W. D. Ristenpart and N. D. Browning, *Acs Nano*, 2012, **6**, 8599-8610.
64. H. M. Zheng, R. K. Smith, Y. W. Jun, C. Kisielowski, U. Dahmen and A. P. Alivisatos, *Science*, 2009, **324**, 1309-1312.
65. I. Hurbain and M. Sachse, *Biology of the Cell*, 2011, **103**, 405-420.
66. J. R. Lawrence, G. D. W. Swerhone, G. G. Leppard, T. Araki, X. Zhang, M. M. West and A. P. Hitchcock, *Applied and Environmental Microbiology*, 2003, **69**, 5543-5554.
67. R. D. Leapman and S. Q. Sun, *Ultramicroscopy*, 1995, **59**, 71-79.
68. S. Q. Sun, S. L. Shi, J. A. Hunt and R. D. Leapman, *Journal of Microscopy-Oxford*, 1995, **177**, 18-30.
69. E. Duke, K. Dent, M. Razi and L. M. Collinson, *Journal of microscopy*, 2014, **255**, 65-70.
70. E. M. H. Duke, M. Razi, A. Weston, P. Guttmann, S. Werner, K. Henzler, G. Schneider, S. A. Tooze and L. M. Collinson, *Ultramicroscopy*, 2014, **143**, 77-87.
71. D. B. Peckys and N. de Jonge, *Microscopy and Microanalysis*, 2014, **20**, 346-365.
72. R. C. Hunter, A. P. Hitchcock, J. J. Dynes, M. Obst and T. J. Beveridge, *Environmental Science & Technology*, 2008, **42**, 8766-8772.
73. J. J. Dynes, M. Obst, M. M. West, A. P. Hitchcock, G. D. Swerhone, J. R. Lawrence, G. G. Leppard, D. R. Korber, K. Kaznatcheev and C. Karunakaran, in *CLS Activity Report 2005-2006*, 2006, pp. 116-118.
74. K. Kaznacheyev, A. Osanna and B. Winn, 6th International Conference on X-Ray Microscopy, Berkeley, Ca, 1999.
75. D. T. L. Alexander, J. R. Anderson, L. Forro and P. A. Crozier, Microscopy and Microanalysis, 2008, vol. 14(Suppl 2), pp. 674-675.
76. A. Braun, F. E. Huggins, N. Shah, Y. Chen, S. Wirick, S. B. Mun, C. Jacobsen and G. P. Huffman, *Carbon*, 2005, **43**, 117-124.
77. E. Najafi, J. A. Wang, A. P. Hitchcock, J. W. Guan, S. Denommee and B. Simard, *Journal of the American Chemical Society*, 2010, **132**, 9020-9029.
78. A. E. Goode, N. D. M. Hine, S. Chen, S. D. Bergin, M. S. P. Shaffer, M. P. Ryan, P. D. Haynes, A. E. Porter and D. W. McComb, *Chemical Communications*, 2014, **50**, 6744-6747.
79. K. Suenaga and M. Koshino, *Nature*, 2010, **468**, 1088-1090.
80. E. G. Rightor, A. P. Hitchcock, H. Ade, R. D. Leapman, S. G. Urquhart, A. P. Smith, G. Mitchell, D. Fischer, H. J. Shin and T. Warwick, *Journal of Physical Chemistry B*, 1997, **101**, 1950-1960.
81. D. E. Luzzi and B. W. Smith, *Journal of Applied Physics*, 2001, **90**, 3509-3515.
82. J. Wang, G. A. Button, M. M. West and A. P. Hitchcock, *Journal of Physical Chemistry B*, 2009, **113**, 1869-1876.
83. J. G. Zhou, J. Wang, C. L. Sun, J. M. Maley, R. Sammynaiken, T. K. Sham and W. F. Pong, *J Mater Chem*, 2011, **21**, 14622-14630.

Nanoscale Accepted Manuscript

84. O. Stephan, M. Kociak, L. Henrard, K. Suenaga, A. Gloter, M. Tence, E. Sandre and C. Colliex, *Journal of Electron Spectroscopy and Related Phenomena*, 2001, **114**, 209-217.
85. A. Felten, C. Bittencourt, J. J. Pireaux, M. Reichelt, J. Mayer, D. Hernandez-Cruz and A. P. Hitchcock, *Nano Lett*, 2007, **7**, 2435-2440.
86. R. J. Nicholls, D. A. Pankhurst, G. A. Botton, S. Lazar and D. J. H. Cockayne, Institute-of-Physics-Electron-Microscopy and Analysis-Group Conference (EMAG 2003), Oxford, ENGLAND, 2003.
87. B. Watts, W. J. Belcher, L. Thomsen, H. Ade and P. C. Dastoor, *Macromolecules*, 2009, **42**, 8392-8397.
88. A. E. Porter, M. Gass, K. Muller, J. N. Skepper, P. Midgley and M. Welland, *Environmental Science & Technology*, 2007, **41**, 3012-3017.
89. M. M. van Schooneveld, A. Gloter, O. Stephan, L. F. Zagonel, R. Koole, A. Meijerink, W. J. M. Mulder and F. M. F. de Groot, *Nature Nanotechnology*, 2010, **5**, 538-544.
90. F. I. Allen, M. Watanabe, Z. Lee, N. P. Balsara and A. M. Minor, *Ultramicroscopy*, 2011, **111**, 239-244.
91. V. J. Keast and M. Bosman, *Microsc. Res. Tech.*, 2007, **70**, 211-219.
92. M. Lerotic, C. Jacobsen, T. Schafer and S. Vogt, *Ultramicroscopy*, 2004, **100**, 35-57.
93. M. Bosman, M. Watanabe, D. T. L. Alexander and V. J. Keast, *Ultramicroscopy*, 2006, **106**, 1024-1032.
94. A. Osanna and C. Jacobsen, *X-Ray Microscopy, Proceedings*, 2000, **507**, 350-357.

Nanoscale Accepted Manuscript

This journal is © The Royal Society of Chemistry [year]